Surface tension driven flow of blood in a rectangular microfluidic channel: Effect of erythrocyte aggregation (EP)

D. Pasias (iD), A. Passos (iD), G. Constantinides (iD), S. Balabani (iD), and E. Kaliviotis (iD)

COLLECTIONS

(EP) This paper was selected as an Editor's Pick

View Online   Export Citation   CrossMark

ARTICLES YOU MAY BE INTERESTED IN

Surface tension driven flow of blood in a rectangular microfluidic channel: Effect of erythrocyte aggregation EP

D. Pasias,[1] G. Constantinides,[1] A. Passos,[2] S. Balabani,[2] and E. Kaliviotis[1,a]

AFFILIATIONS

[1] Department of Mechanical Engineering and Materials Science and Engineering, Cyprus University of Technology, 45 Kitiou Kyprianou, 3041 Limassol, Cyprus

[2] Department of Mechanical Engineering, University College London, Roberts Building, Torrington Place, WC1E 7JE London, United Kingdom

[a] Author to whom correspondence should be addressed: e.kaliviotis@cut.ac.cy

ABSTRACT

Microfluidic platforms have increasingly been explored for *in vitro* blood diagnostics and for studying complex microvascular processes. The perfusion of blood in such devices is typically achieved through pressure-driven setups. Surface tension driven blood flow provides an alternative flow delivery option, and various studies in the literature have examined the behavior of blood flow in such fluidic devices. In such flows, the influence of red blood cell (RBC) aggregation, the phenomenon majorly responsible for the non-Newtonian nature of blood, requires particular attention. In the present work, we examine differences in the surface tension driven flow of aggregating and non-aggregating RBC and Newtonian suspensions, in a rectangular microchannel. The velocity fields were obtained using micro-PIV techniques. The analytical solution for blood velocity in the channel is developed utilizing the power law model for blood viscosity. The results showed that RBC aggregation has an impact at the late stages of the flow, observed mainly in the bluntness of the velocity profiles. At the initial stages of the flow, the shearing conditions are found moderately elevated, preventing intense RBC aggregate formation. As the flow decelerates in the channel, RBC aggregation increases, affecting the flow characteristics.

Published under license by AIP Publishing. https://doi.org/10.1063/5.0008939

NOMENCLATURE

ΔP_{Y-L}	Young–Laplace pressure difference (Pa)
$\lvert\dot{\gamma}\rvert$	shear rate magnitude (s^{-1})
$\dot{\gamma}_{i-p}$	in plane shear rate component (s^{-1})
ε	relative threshold value (-)
θ_c	static contact angle (deg.)
θ_d	dynamic contact angle (deg.)
μ	dynamic viscosity (mPa)
μ_{NF}	Newtonian fluid dynamic viscosity (mPa)
μ_{P_L}	power law viscosity (mPa)
ρ	density (Kg m^{-3})
σ	surface tension (N m^{-1})
ω	angular velocity (rad s^{-1})
AR	aspect ratio (W/h) (-)
Ca	capillary number (-)
CO_2	carbon dioxide (-)
CV	coefficient of variation (-)
D	depth of correlation (μm)
d_h	hydraulic diameter (μm)
d_p	particle diameter (μm)
h	half height of the channel (μm)
h_p	gap between the plates (μm)
$\bar{I}$	mean intensity (-)
k	power law consistency index (Pa s^n)
L_e	entrance length (μm)
L_w	wavelength of illumination (μm)
L(t)	time-dependent meniscus position (μm)
M	image magnification (-)
n	power law index (-)
N	refractive index of air (-)
NA	numerical aperture (-)

NAB	non-aggregative blood (-)
NF	Newtonian fluid (-)
O_2	oxygen (-)
P	pressure (Pa)
PBS	phosphate buffered saline (-)
PIV	particle image velocimetry (-)
Q	flow rate per unit length ($\mu m^2\ s^{-1}$)
r	radius (μm)
R_1, R_2	radii of the meniscus curvature (μm)
ROI	region of interest (-)
SD	standard deviation (-)
SD_I	intensity standard deviation (-)
St	Stokes number (-)
STD	surface tension driven (flow) (-)
t	time (s)
t_p	particle response time (s)
t_f	flow characteristic time (s)
TiO_2	titanium dioxide (-)
UV	ultraviolet (-)
v	linear velocity (plate flow) ($\mu m\ s^{-1}$)
V_{max}	maximum of V_{ch} ($\mu m\ s^{-1}$)
V_c^*	normalized blood velocity in the Couette flow (-)
V_{ch}	velocity in the core of the channel ($\mu m\ s^{-1}$)
$\bar{V}_{ch}$	mean of V_{ch} ($\mu m\ s^{-1}$)
V_{ch}^*	V_{ch} normalized with V_{max} (-)
V_m	mean meniscus velocity ($\mu m\ s^{-1}$)
$\bar{V}_m$	mean value of V_m ($\mu m\ s^{-1}$)
$V_{m\text{-}an}$	theoretical meniscus velocity ($\mu m\ s^{-1}$)
V_{mean}	theoretical mean core-flow velocity ($\mu m\ s^{-1}$)
$\bar{V}_{m\text{-}mean}$	mean of $\bar{V}_m$ ($\mu m\ s^{-1}$)
V_p^*	normalized plate velocity (-)
$V_{z\text{-}c}$	velocity in the flow core, z-dir. ($\mu m\ s^{-1}$)
$V_{z\text{-}\sigma}$	theoretical velocity profile, z-dir. ($\mu m\ s^{-1}$)
W	width of the channel (μm)
WB	whole blood (-)
x^*	normalized x-dir. ($x^* = x/W$) (-)
y^*	normalized y-dir. ($y^* = y/W$) (-)
z^*	normalized z-dir. ($z^* = z/W$) (-)

I. INTRODUCTION

Microfluidic technology has received considerable attention over the last decades.[1] Microfluidic devices allow for small sample manipulation and enable miniaturization of laboratory techniques. Such devices have become increasingly popular in diagnostics and health care applications due to a number of advantages:[2] They are cost effective, can be used on site, and are disposable, making them very practical for research and clinical use.[3] Furthermore, they offer tremendous potential in areas such as drug discovery, biosensing, and chemical synthesis, where handling small volumes is critical.[4]

Microfluidic studies designed to mimic the microcirculation and probe the flows therein utilize, by default, pressure-driven experimental setups. Pioneering studies using fluorescent and brightfield particle image velocimetry techniques allowed the detailed analysis of the flow in such applications.[5,6] Lima et al.[7,8] examined the effect of hematocrit (Hct) on microscale blood flow

by utilizing confocal micro-PIV techniques, using non-aggregating samples in a square microchannel. The velocity profiles were found parabolic, with considerable velocity fluctuations observed at increased hematocrits. The radial displacement of red blood cells (RBCs) flowing through a tube of 100 μm diameter was also examined; it was found that RBCs exhibit higher erratic radial displacement in dense (24%–35% Hct) compared to dilute suspensions.[8] The flow and the structural/mechanical characteristics of blood in bifurcating microchannels (T-type) were examined in a series of studies by the authors in Refs. 9–14 using aggregating and non-aggregating RBC suspensions; the flow split ratio between the parent and daughter branches was found to affect the hematocrit (and RBC flux), the aggregate size distribution (and aggregate flux), and the local viscosity of the fluid. Furthermore, RBC aggregation was found to increase the bluntness and skewness of the velocity profiles and the properties of the cell depleted layer (CDL). Studies have shown that RBC clustering, which was not caused by RBC aggregation forces, takes place in confined flows[15] and that the therapeutic efficacy of microparticles used in drug delivery could be affected by the particle/RBC interaction in the vasculature.[16] The effect of RBC aggregation on microscale blood flows has also been examined in a straight microchannel by Mehri et al.,[17,18] illustrating the relationship between aggregate size, shear rate, and viscosity and in an artificial microvascular network[19] showing no effect of RBC aggregation on perfusion, but a hematocrit increase in the capillary scale branches of the network.

Pressure-driven flows require accurate pumping and tubing, which may cause various difficulties for point of care diagnostics.[20] Surface tension driven (STD) blood flow offers a simpler and cost effective option to the pressure-driven flows.[4,21] Surface tension is a material property of a fluid–fluid interface whose origins lie in the different attractive intermolecular forces that act in the two fluid phases. STD flows depend on the hydrophilicity/hydrophobicity of the surface material. Hydrophilic materials have good affinity with fluids causing them to spread, whereas hydrophobic materials cause repulsion to fluids resulting in droplet formation.[22] Various methods have been employed to improve the surface properties of the channel materials. The hydrophilicity of the surfaces can be improved with low power laser CO_2 ablation,[23] oxygen plasma exposure,[24,25] and ultraviolet (UV) surface activation.[26] Surface wetting properties induced by plasma can be maintained for a few weeks.[27] Combining TiO_2 films with O_2 plasma etching treatment and/or UV activation[28] has been found to further enhance the wetting properties of glass surfaces.

In addition to surface treatment strategies, geometrical characteristics such as aspect ratio (AR) and turning angle are important in designing microchannels for STD flows. These characteristics have been examined in various studies, and it has been shown that as the aspect ratio increases, the velocity of the advancing liquid front increases for AR up to 1.5.[29–32] Chen et al.[29] also examined the flow characteristics in open microchannels with different turning angles (45°–135° with respect to the horizontal plane) for Newtonian fluids; they reported that the meniscus decelerated at the turning region and accelerated immediately after (for the 90°–135° angles) reaching higher velocities than the incoming flow, before recovering back to its original incoming velocity.

Berthier et al.[20] studied the spontaneous capillary blood flow in a narrow V-groove microchannel, and the maximum measured velocities were found to be up to 7.5 cm/s, decreasing non-linearly with time and distance, but remaining at relatively high magnitudes for a significant proportion of the channel length. Experimental observations agreed with the theoretical analysis of spontaneous capillary flows in open V-groove channels, based on a force balance between the capillary forces driving the flow and the viscous friction at the walls resisting the flow. Kung et al.[30] studied STD blood flow in an inclined microchannel at different sloping angles (from $-90°$ to $+90°$). Surprisingly, it was found that the blood flow rate was increased for the upward motion (angle $> 0°$) while decreasing for the downward flow (angles $< 0°$). This was explained by the change in frictional force at different sloping angles, due to the hematocrit decrease in the upward flow case. Cito et al.[21] examined the flow behind the advancing meniscus for water and blood using rectangular and circular microchannels of various cross sections and utilizing a spectral-domain Doppler optical coherence tomography technique for the visualization of the flow; they showed that recirculation regions exist behind the meniscus, with developing velocities normal to the flow, which were comparable to and even higher than the meniscus velocities. The results were then compared with the analytical predictions of the Lucas–Washburn equation, assuming that blood behaves as a power-law non-Newtonian fluid and found to be in a reasonable agreement.[21] Other theoretical studies have reported an initial acceleration followed by a flow deceleration as the capillary force is balanced by the inertia forces of the fluid.[32,33] In a computational study analyzing the exit effects on STD blood flow,[34] it was shown that if the capillary tube has an open window at the end, the results agree with those of a simplified analytical solution[32] within 5%. However, in the case that the capillary tube has a side exit opening instead of an opening facing the meniscus front, the effect of the air motion in front of the blood–air interface becomes more significant.

STD flows for diagnostic purposes have also been reported in the literature. Sneha Maria et al.[27] devised a rectangular polydimethylsiloxane (PDMS) microchannel, with differential wetting properties, in order to separate the plasma and detect the glucose levels therein. In another study,[35] an on-chip whole blood (WB)/plasma separator was developed using a combination of asymmetric nanoporous super-hydrophilic surfaces and patterned hydrophobic patches. An asymmetric capillary force through the microchannel was attained to achieve the separation of plasma from whole blood. Red blood cells were continuously accumulated within the hydrophobic patch, which worked as a naturally organized microfilter.[35]

Despite the potential and increasing interest of STD flows in blood flow diagnostics, there are aspects in such flows that have not been systematically investigated to date; key properties of blood such as RBC aggregation have not been considered thoroughly. RBC aggregation is a major determinant of blood viscosity,[36] and it has been shown to affect local microscale flow characteristics.[9] In the present study, we examine the influence of the RBC aggregation phenomenon on surface tension driven flows in rectangular microchannels. Aggregating and non-aggregating blood samples were tested; their flow characteristics were determined using micro-PIV-based techniques and compared to those for a Newtonian fluid flowing in the same channel.

II. METHODOLOGY

A. Sample preparation

The study was approved by the Cyprus Bioethics Committee (ref: ЕЕВК/ЕП/2016/18). Five blood samples were acquired from healthy volunteers into 4 ml vacuum tubes (BD) preloaded with 1.8 mg/ml EDTA. Whole blood (WB) was used for aggregating blood experiments, whereas non-aggregative blood samples (NAB) were produced by washing RBCs twice in Phosphate Buffered Saline (PBS), centrifuging at 3600 rpm for 10 min, and re-suspending them in PBS. WB and NAB samples were both adjusted at a hematocrit of 45% by adding/subtracting plasma. For consistency, all experiments were conducted with a single sample. The consistency was further examined by duplicating/triplicating tests where appropriate. Newtonian flows were also examined using milk/water solutions (1:3 concentration, respectively). Milk particles were used as tracers for the µPIV-based analysis of Newtonian fluids (NFs), as in previous studies.[37]

B. Microfluidic channel fabrication

The microchannel was made of glass slides (Superfrost, 1 mm thickness) and double-sided tape (3M, 100 µm thickness, resulting in 100 µm microchannel height), as shown in Fig. 1, an approach similar to that used in Juncker et al.[38] The aspect ratio (AR = W/h) was ~3, and the channel length was 10 mm. Part of the bottom glass slide was left protruded to accommodate the blood drop. In the present work, the variables x, y, and z are normalized with the width of the channel (W ~ 300 µm) and expressed as x^*, y^*, and z^*. The origin of the coordinate system was taken at the midplane of the channel, at the entrance. All measurements were performed in the region from z = 600 µm from the entrance of the channel to a distance of ~z = 1700 µm to avoid any entrance effects, as in Ref. 21: An entrance length (Le) 3.5 times the channel height (350 µm in the present case) for capillary flow in a rectangular channel is sufficient to ensure fully developed flow.[39]
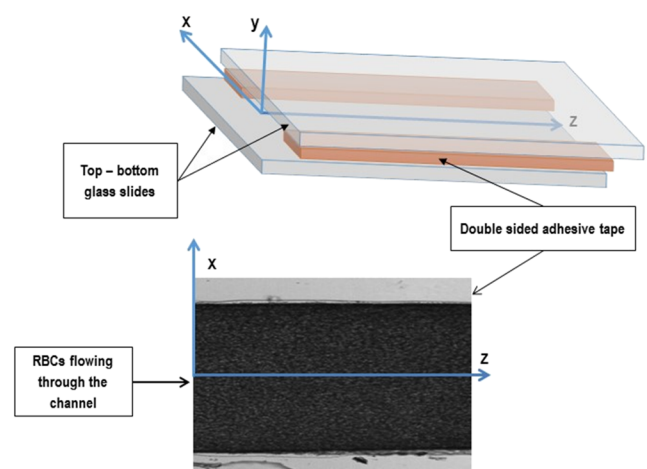

FIG. 1. Top: schematic of the microchannel geometry (not in scale) and the coordinate system used. Bottom: sample image of the RBC flow in the microchannel.
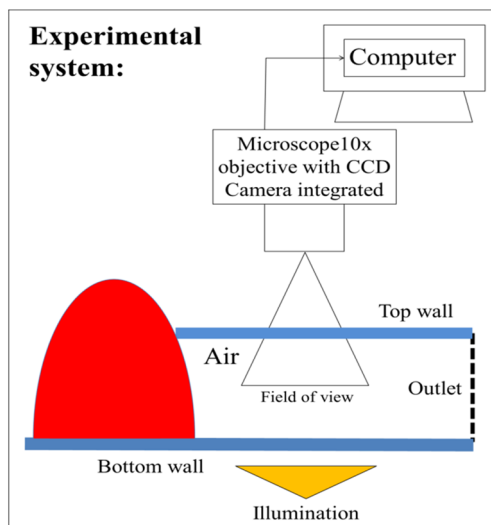
FIG. 2. Annotated schematic of the capillary driven microchannel flow and the μPIV measurement set up: the gap (2h) between the top and bottom walls of the channel was 100 μm, respectively (diagram not to scale).

C. Experimental setup and procedures

Figure 2 shows a schematic of the experimental setup using the brightfield μPIV system. The microchannel was placed horizontally on an upright microscope stage (OLYMPUS BX51). A 50 μl drop of fluid was placed on the protruding part of the bottom glass slide and at the entrance to the channel using a micropipette. The fluid was then set in motion through the channel due to the action of surface tension. The flow was recorded with a CMOS camera (IDT X3, at 625 fps) attached on the microscope (10×-objective NA = 0.25) and analyzed using JPIV (www.jpiv.vennemann-online.de)

and Matlab software. The spatial resolution of the optics was 1.65 μm/pixel.

D. Contact angles and surface tension

Static contact angle measurements were performed by capturing drop images (Fig. 3) at the surfaces of contact (glass and adhesive tape) and then analyzing the images using ImageJ software. The contact angle measurement setup consisted of a universal serial bus (USB) camera, aligned with the XZ surface plane (Fig. 1) of the specimen. Both the camera and the specimen were secured on a horizontally leveled stand. A drop of 10 μl volume was applied with a micropipette on the surface of the specimen. The drop surface and drop contact lines were identified through image processing using software ImageJ. The contact angle θ_c was defined as the angle between the line of contact and the surface line of the drop, measured counterclockwise [Figs. 3(c) and 3(d)]. When the wettability is high, small contact angles ($\ll 90°$) and large base diameters occur [Figs. 3(a)–3(c)], whereas when wettability is low, large contact angles ($\gg 90°$) and smaller base diameters are apparent [Fig. 3(d)].[40]

The static contact angles of the fluids on the hydrophilic glass surfaces were found to be $36°$, $38°$, and $44°$ for the NAB, WB, and NF fluids respectively, forming a drop base diameter of ~5 mm [Figs. 3(a)–3(c)]. Contact angles on the adhesive tape were found to be $100°$, $96°$, and $110°$, for the NAB, WB, and NF fluids, respectively, indicating the neutral/hydrophobic nature of the side, as opposed to the top and bottom walls of the channels [Fig. 3(d)]. The drop base diameters for the aforementioned cases were found to be ~3 mm.

Sample images of the surface tension driven microchannel flows of WB and NF are shown in Fig. 3(e). The angle that the marching meniscus forms with the side-walls of the channel (the adhesive tape) is the dynamic contact angle, denoted by θ_d, which is also an index of wettability.[40] In the present case, θ_d was calculated from the meniscus profile at each time step. A best line of fit was created at the meniscus profile close to the side-wall, and θ_d was evaluated using $\theta_d = \tan^{-1}\frac{\Delta x}{\Delta z}$. The meniscus is seen
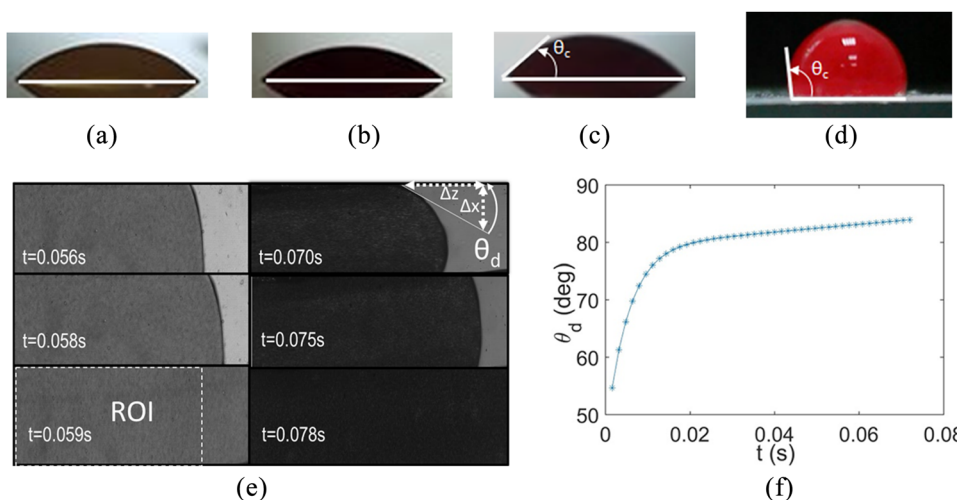

FIG. 3. Top panels: images of drops from the Newtonian fluid (a), the non-aggregating blood (b), and whole blood (c) on the glass surface. θ_c is the measured static contact angle. Panel (d): representative image of a whole blood drop on the adhesive tape. Panel (e): images of whole blood (right) and Newtonian fluid flow (left), showing the meniscus shape and the region of interest in which the velocity profiles were derived; the dynamic contact angle is shown on the top-right channel. Panel (f): dynamic contact angle θ_d (in degrees) as a function of time.

to have a slight paraboloid or even a uniform shape due to the non-hydrophilic properties of the side-walls (double-sided adhesive tape). Figure 3(f) shows a representative dynamic contact angle θ_d against time, illustrating that the meniscus profile becomes nearly flat as the dynamic contact angle reaches $\sim 85°$ very shortly. The hydrophobicity/neutrality of the side boundaries does not promote the meniscus flow, which is driven by the surface tension forces developed at the top and bottom boundaries; it should be noted that the top/bottom dynamic contact angles could not be measured in the current setup.

Surface tension values were measured for each fluid using a Kruus 100 surface tensiometer and found to be 0.022 Nm^{-1}, 0.023 Nm^{-1}, and 0.020 Nm^{-1} for the NF, NAB, and WB respectively.

E. µPIV processing

A representative image of the flow of blood in the microchannel configuration is shown in Fig. 1. The images were processed using the open source software JPIV to resolve the velocity field, and Matlab software was used for the analysis of the data. Three passes with interrogation windows (IW) of height and width of 32 and 16, and 8 pixels were used for the µPIV processing on the acquired images. Invalid vectors were replaced by the median of the neighboring vectors. In the present study, a 13.2 µm vector spacing (for $10\times$ magnification) was achieved. Velocity profiles were calculated by axially averaging all of the velocities in a region of interest (ROI) after the meniscus had progressed in the channel.

F. Validation of the µPIV technique

It is well established that brightfield micro-PIV techniques suffer from relatively large depth of correlation fields (D),[41] which lead to an underestimation of the velocity magnitude. Poelma et al.[42] have shown that for relatively low magnifications in the µPIV setup, the measured velocity is 33% lower than the actual flow velocity. D can be estimated using the following equation:[41]

$$D = 2\left[\frac{(1-\sqrt{\varepsilon})}{\sqrt{\varepsilon}}\left\{\frac{N^2 d_p^2}{4NA^2}\right\} + \left\{\frac{5.95(M+1)^2 L^2 N^4}{16M^2 NA^4}\right\}\right]^{\frac{1}{2}}, \quad (1)$$

where d_p is the particle diameter, L_w is the wavelength of illumination, M is the image magnification, N is the refractive index of air, and NA is the numerical aperture of the lens. ε is the relative threshold over which particles no longer contribute to the evaluation of the displacement–correlation peak, which normally takes the value of 0.01. Hence, it can be considered that the measured velocity information represents the mean velocity of RBCs in the depth D, as the latter was calculated to be 99 µm.

In order to assess the brightfield µPIV technique employed in the present study, three methods were utilized. In the first method, the velocity of RBCs (45% concentration) in a plate–plate system (CSS450 LINKAM SCIENTIFIC, see Fig. 4 for a diagrammatic representation) was measured experimentally and compared with the analytical solution for the particular flow. More specifically, a thin film (~ 150 µm) of whole blood was applied at the bottom plate of the plate–plate system of Fig. 4. The upper plate of the system was not placed, and the bottom plate was then rotated at different constant rotational speeds ($\omega = 0.13$ rad s^{-1} and 0.8 rad s^{-1}). The velocity
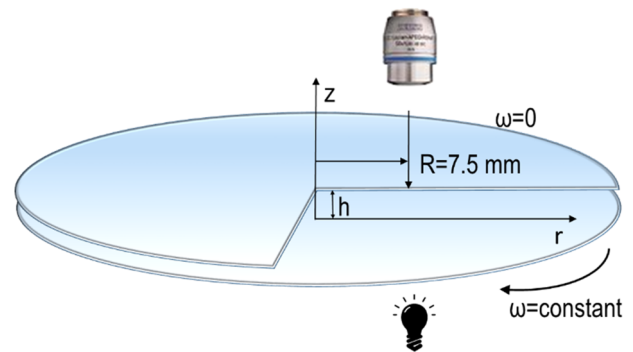

FIG. 4. Schematic of the plate–plate system.

field was determined from the acquired images using JPIV. The linear velocity of the plate in the area of observation is given by $v = \omega r$ for a range of radius r, from r = 7.1 mm to r = 7.9 mm, and a constant angular velocity ω.

In the second method, simple Couette flows were generated between the bottom and the upper plate of the system (with the gap between the plates set at $h_p = 100$ µm). The blood sample was placed between the plates, and the microscope was focused at a height of 50 µm from the bottom plate. The bottom plate was rotated at two angular speeds ($\omega = 0.13$ rad s^{-1} and 0.8 rad s^{-1}) producing shear rates of 10 s^{-1} and 60 s^{-1} respectively. µPIV measurements were performed as described previously.

The expected velocity profile for a narrow gap of h = 50 µm was also calculated analytically for the lower plate rotating at an angular velocity ω and the upper plate held stationary,

$$v = r\omega\left(1 - \frac{z}{h_p}\right), \quad (2)$$

with z = 50 µm and r ranging from 7.1 mm to 7.9 mm.

Figures 5(a) and 5(b) compare the measured velocity profiles against the theoretical one for the first validation method (thin film of blood rotating on plate), illustrating good qualitative agreement (velocity data have been normalized with their values at the center of the flow). Absolute velocity values were lower than the theoretical ones by $\sim 10\%$ and $\sim 30\%$ for the 0.13 rad s^{-1} and 0.8 rad s^{-1} angular velocities, respectively. Figures 5(c) and 5(d) show the comparison between measured and analytical normalized velocities for the Couette flow developed in the gap of the shearing system. The angular velocities were kept the same as in the previous test case, 0.13 rad s^{-1} and 0.8 rad s^{-1}, resulting in the shear rates of 10 s^{-1} and 60 s^{-1}; the observed velocity underestimation was $\sim 20\%$ and $\sim 30\%$, respectively. The underestimation in the velocity magnitude calculated with the µPIV technique is $\sim 30\%$ maximum, in agreement with the discrepancies reported in other studies.[42] The large depth of field, D, also means that the flow regions closer to the objective will contribute more to the PIV analysis than the regions further away. The velocities in these regions are smaller (since they are closer to the top, fixed plate), which might further bias the measured (underestimated) velocities.[42]
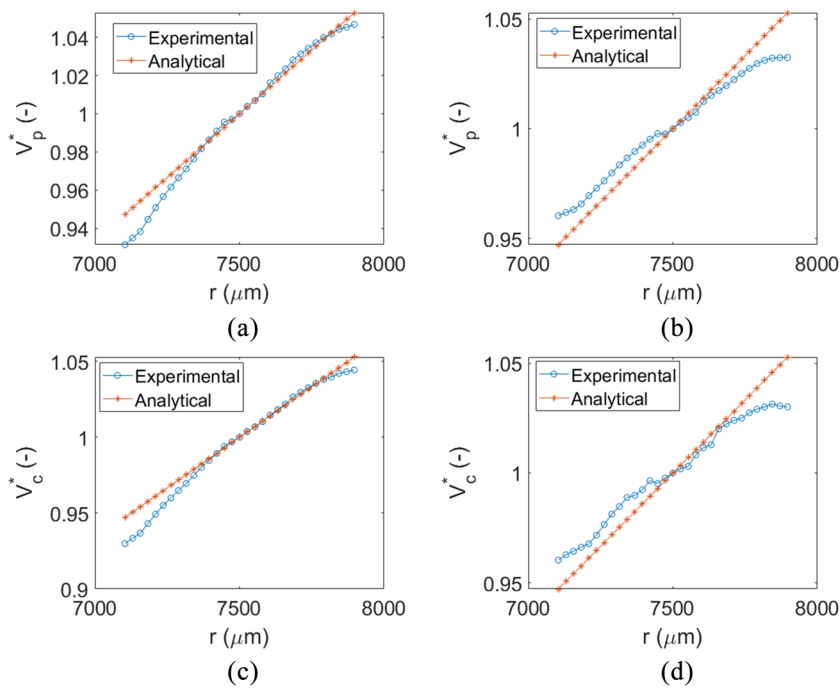
FIG. 5. Top panels: experimental vs analytical velocity V_p^* (normalized with velocity values at the center of the flow) for whole blood rotating on the bottom plate at $\omega = 0.13$ rad/s (a) and $\omega = 0.8$ rad/s (b) (absolute velocities differ by 10.30% and 30.52%, respectively). Bottom panels: experimental vs analytical velocity V_c^* (normalized with velocity values at the center of the flow) derived from the Couette flow with shear rates 10 s^{-1} ($\omega = 0.13$ rad/s) (c) and 60 s^{-1} ($\omega = 0.8$ rad/s) (d) (absolute velocities differ by 21.06% and 28.46%, respectively).

In a third validation exercise, the velocity field of the Newtonian STD flow in a microchannel (AR ~ 3.7) was measured, utilizing a laser based micro-PIV technique using fluorescent particles as tracers (Nile Red, ~1 μm size, at 1% concentration) suspended in distilled water, and compared against brightfield μPIV measurements (JPIV software) using milk particles as tracers in a 1:3 milk/water Newtonian solution. The experimental setup for the fluorescent μPIV experiments is described in previous studies by Zhang et al.[43,44] The system comprised a 16 Hz Nd:YAG laser source at 532 nm (Litron Laser, UK), for illumination, and a sCMOS camera (Xyla 5.5, Andor, UK) integrated on a bespoke microscope assembly (10× objective, NA = 0.28), for image acquisition. The spatial resolution of the technique was 0.56 μm/pixel, and

the depth of the correlation was estimated to cover the entire flow depth.

Figure 6(a) shows an annotated schematic of the laser based μPIV system, and Fig. 6(b) compares the measured velocity profiles (both profiles are normalized by the maximum measured velocity). Qualitatively, the two profiles show very good agreement. The slightly increased bluntness of the velocity profile measured with the laser micro-PIV technique could be attributed to technique-specific issues (differences in correlation depth, etc.). The decrease in the velocity gradient near the side-walls of the channel is mainly due to the non-uniformity of the side-walls of the channels (adhesive tape), in which existing micro-pockets created regions of persistently low velocity. A direct comparison of velocity magnitudes between the
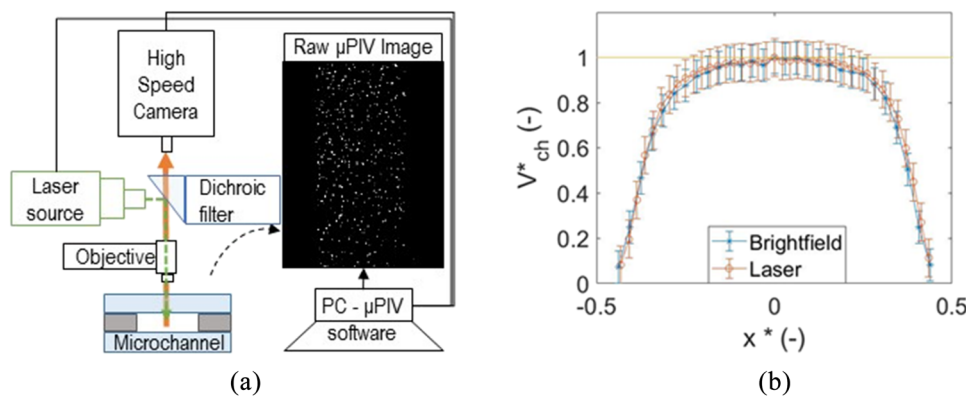

FIG. 6. (a) Annotated schematic of the laser micro-PIV and an enhanced raw PIV image. (b) Normalized velocity profiles of a Newtonian fluid flow measured with brightfield (blue stars) and laser micro-PIV (orange circles).

measurement techniques shows a maximum difference of ~15% with the velocity in fluorescent μPIV being higher.

The Stokes number of the tracer particles can be calculated from $St = \frac{t_p}{t_f}$, where t_p is the particle characteristic response time, given by $t_p = \frac{\rho_p d_p^2}{18\mu_{NF}}$, with a particle density $\rho_p = 1050$ kg m^3, particle nominal diameter $d_p = 1$ μm, and Newtonian fluid viscosity $\eta_{NF} \approx 1.68\ 10^{-3}$ Pa s (see Sec. II G for information on viscosity measurements).[45] t_f is a flow characteristic time defined as $t_f = \frac{d_h}{\bar{V}_{PIV}}$. $\bar{V}_{PIV}$ is the mean velocity of the flow, calculated by the PIV technique here and found to be in the order of 3 mm s^{-1}, and d_h is a characteristic diameter (hydraulic) of the channel equal to 150 μm. St was found to be on the order of 10^{-8}, indicating a negligible particle response time to the dynamics of the flow, hence indicating that the particles following the flow faithfully.

G. Viscosity measurements

Viscosity measurements were performed using a Brookfield DVIIT instrument, utilizing a cone-plate geometry. Samples were loaded in the plate of the viscometer with a micropipette (0.6 ml volume), and tests were initiated ~30 s afterward. Viscosities were measured by ramping down shear rates from 400 s^{-1} to 12.5 s^{-1}, in order to ensure initial RBC aggregate dispersion. The maximum shear stress that cells were exposed at the highest shear rate was ~2 Pa for 30 s. The duration of a complete viscosity test was 8 min (16 points of measurement for 30 s each), and the viscosity measurement was performed at the end of the shearing period at each point. All measurements were performed at room temperature (25 ± 0.5 °C). A power law model was used to fit the data from the viscosity measurements ($\mu_{P\_L} = k\dot{\gamma}^{n-1}$).[46]

Viscosity curves of the three working fluids are shown in Fig. 7 for shear rates ranging from 12.5 s^{-1} to 400 s^{-1}. As expected, whole blood exhibits a shear thinning behavior mainly due to RBC aggregation. The non-aggregating sample (RBCs in PBS medium) exhibits a smaller decrease in viscosity with an increasing shear rate, which is mainly due to the deformation of RBCs. The viscosity of the
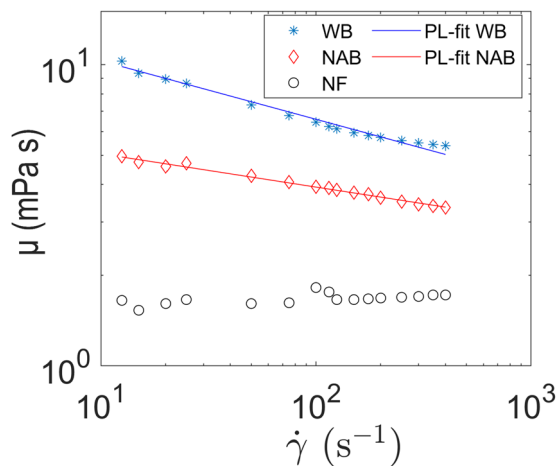

FIG. 7. Viscosity of WB (stars), NAB (diamonds), and NF (circles) at shear rates from 12.5 s^{-1} to 400 s^{-1}.

TABLE I. Power law coefficients and R^2 values of blood samples.

Sample	k (mPa s^n)	n	R^2
WB	26.200	0.302	0.973
NAB	7.134	0.123	0.991

Newtonian solution is effectively constant at ~1.68 mPa s. The power law viscosity model ($\mu_{P\_L} = k\dot{\gamma}^{n-1}$) was used to fit the viscosity data for both the WB and NAB blood suspensions, similarly to other studies.[46] The consistency indices k and the exponent n for the WB and NAB cases are shown in Table I and are in agreement with the reported values in the literature.[46]

H. Analytical solutions

1. Mean meniscus velocity

The theoretical mean axial (z-direction) meniscus velocity in STD flows can be calculated analytically as in previous studies,[21,47] using the incompressible Navier–Stokes (N–S) equations, under the assumptions that the flow is fully developed and one-dimensional, influenced mainly by the smaller dimension of the geometry (i.e., the height, 2h, of the channel, in the y-direction for the coordinate system chosen for this study). The latter is due to the smaller radius of the meniscus curvature in the y-direction, compared to the one in the width direction (x). Under these assumptions, the continuity and z-momentum equations in the N–S equations reduce to

$$\frac{\partial V_{z-\sigma}}{\partial z} = 0 \tag{3}$$

and

$$-\frac{1}{\rho}\frac{\partial P}{\partial z} + \frac{\mu}{\rho}\frac{\partial^2 V_{z-\sigma}}{\partial y^2} = 0, \tag{4}$$

where μ is the dynamic viscosity of the fluid and $\partial P = P_1 - P_0$. However, since the chancel is open ended, P_1 is equal to the atmospheric pressure, resulting in $\partial P = -P_0$, leading to $\frac{\partial P}{\partial z} = \frac{-P_0}{L}$, with L the meniscus position from the entrance. ∂P can be approximated with the Young–Laplace pressure drop,

$$\Delta P = \sigma\left(\frac{1}{R_1} + \frac{1}{R_2}\right), \tag{5}$$

where R_1 and R_2 are the radii of curvature on the top and side-walls of the channel, respectively. As mentioned above, due to the high aspect ratio of the channel, the radius of curvature along the width W is much higher, compared to that along the height 2h; hence, the term $1/R_2$ is small compared to $1/R_1$ and considered negligible. This assumption results in $\Delta P_{Y-L} = \frac{2\sigma\cos(\theta_c)}{2h}$ and, therefore,

$$-\frac{\partial P}{\partial z} = \frac{\sigma\cos(\theta_c)}{hL}. \tag{6}$$

Inserting Eq. (6) into Eq. (4) yields

$$\frac{\sigma\cos(\theta_c)}{hL} + \mu\frac{\partial^2 V_{z-\sigma}}{\partial y^2} = 0. \tag{7}$$

Integrating Eq. (7) once and applying the condition $\frac{\partial V_{z-\sigma}}{\partial y} = 0$ at y = 0 for a velocity maximum at the center of the channel yields

$\mu \frac{\partial V_{z-\sigma}}{\partial z} = -\frac{\sigma \cos(\theta_c)}{hL} y$. By using the power law shear stress $\mu \frac{\partial V_{z-\sigma}}{\partial y} = k[\frac{\partial V_{z-\sigma}}{\partial y}]^n$, the equation becomes $k[\frac{\partial V_{z-\sigma}}{\partial y}] = -(\frac{\sigma \cos(\theta_c)}{hkL})^{1/n}$ and can be solved using the no-slip boundary condition at the wall $V_{z-\sigma} = 0$ at $y = h$,

$$V_{z-\sigma} = \left(\frac{n}{n+1}\right)\left[\frac{\sigma \cos(\theta_c)}{khL}\right]^{\frac{1}{n}}\left[h^{1+\frac{1}{n}} - y^{1+\frac{1}{n}}\right]. \quad (8)$$

For $n = 1$, the parabolic Newtonian profile is recovered. The flow rate can be calculated from the velocity profile $V_{z-\sigma}$,

$$Q = 2W \int_0^h V_{z-\sigma} dy$$
$$= 2W\left(1 + \frac{1}{n}\right)\left[\frac{\sigma \cos(\theta_c)}{khL}\right]^{\frac{1}{n}}\left[h^{\frac{2n+1}{n}}\left(1 - \frac{n}{2n+1}\right)\right]. \quad (9)$$

The mean velocity in the core of the flow can be calculated as $V_{mean} = Q/hW$,

$$V_{mean} = \left(1 + \frac{1}{n}\right)\left[\frac{\sigma \cos(\theta_c)}{hkL}\right]^{\frac{1}{n}}\left[h^{\frac{n+1}{n}}\left(1 - \frac{n}{2n+1}\right)\right]. \quad (10)$$

Assuming that the mean velocity of the meniscus (V_m) is equal to the mean velocity in the core of the flow (i.e., $V_m = V_{mean}$), the meniscus position as a function of time [$L = L(t)$] can be estimated using

$$\frac{dL(t)}{dt} = V_{mean}. \quad (11)$$

Therefore,

$$L(t) = h\left[\frac{\sigma \cos(\theta_c)}{hk}\right]^{\frac{1}{n+1}}\left[1 - \frac{n}{2n+1}\right]^{\frac{n}{n+1}} t^{\frac{n}{n+1}}. \quad (12)$$

The time-dependent marching meniscus velocity can be estimated analytically from the position L(t),

$$V_{m\text{-}an} = \frac{dL(t)}{dt} = ht^{\left(\frac{-1}{n+1}\right)}\left[\frac{\sigma \cos(\theta)}{kh}\right]^{\frac{1}{n+1}}\left[\frac{n}{n+1}\right]\left[1 - \frac{n}{2n+1}\right]^{\frac{n}{n+1}}. \quad (13)$$

The solution for the mean meniscus velocity ($V_{m\text{-}an}$) is similar to other solutions in the literature[21] for the flow in the circular capillary duct.

2. Two-dimensional velocity profile in the core of the flow

The mean meniscus velocity was derived in Sec. II H 1 based on Eq. (8), assuming a negligible influence from the side boundaries [i.e., $V_{z-\sigma} = V_{z-\sigma}(y)$]. For the analysis of the velocity field in the core of the flow, however, a complete analytical solution in both x-direction and y-direction is required to compare with the experimental data. The two-dimensional analytical solution for the velocity of pressure-driven flows in straight rectangular microchannels exists for a Newtonian fluid.[47] The boundary conditions in such a case also require zero velocity at all boundaries, i.e., $V_z = 0$ at $x = \pm W/2$ and at $y = 0$ and $2h$ (bottom and top plate for this solution), which are satisfied using a Fourier series expanded along the short, vertical y-direction.[47] For the central plane of the microchannel and when the Young–Laplace pressure is used as the flow driving

TABLE II. Young–Laplace pressure and the pressure/viscosity ratio for the three working fluids.

Sample	σ (Nm^{-1})	θ_c (deg)	μ (mPa s)	ΔP_{Y-L} (Pa)	$\Delta P_{Y-L}/\mu$ (s^{-1})
WB	0.020	38	8	315.2	39.4×10^{-3}
NAB	0.023	36	4.41	372.1	84.4×10^{-3}
NF	0.022	44	1.68	316.5	188.4×10^{-3}

mechanism, the solution for the central plane in the geometry takes the following form:

$$V_{z-c} = 8W^2 \frac{\sigma \cos\theta_c}{\pi^3 \mu 2hL} \sum_{n,odd}^{\infty} \frac{1}{n^3}\left[1 - \frac{\cosh\left(n\pi\frac{y}{2h}\right)}{\cosh\left(\frac{n\pi}{2}\right)}\right]. \quad (14)$$

The value of L can be set from the experimental data or from Eq. (12) and will affect the behavior of V_{z-c} quantitatively. The analytical solution V_{z-c} will be used to assess the deviation of the experimental velocity profiles from the Newtonian behavior. The viscosity values used were 1.68 mPa s, 4.41 mPa s, and 8 mPa s, i.e., the mean values for the NF, NAB, and the WB samples, respectively.

I. Pressure–viscosity ratio

The main factors influencing the velocity of the flow are the surface tension σ, the viscosity of the fluids μ, and the wettability of the top-bottom channel surfaces quantified by the contact angle θ_c. The surface tension σ and wettability (contact angle θ_c) can be used to calculate the Young–Laplace pressure difference ΔP_{Y-L} using $\Delta P_{Y-L} = \frac{\sigma \cos(\theta_c)}{h}$. The ratio $\Delta P_{Y-L}/\mu$ could provide meaningful information about the interrelationships between the aforementioned factors. Table II shows that the pressure/viscosity ratio is found to be higher in the NF fluid (188.4×10^{-3} s^{-1}), compared to NAB and WB (84.4×10^{-3} and 39.4×10^{-3} s^{-1}, respectively). Thus, the flow of NF is expected to be favored compared to the other fluids, with WB been affected mostly by the higher viscosity. Table II shows the measured and aforementioned quantities in comparison.

III. RESULTS AND DISCUSSION

A. Meniscus velocity

The meniscus velocity (V_m) was calculated for the initial stages of the flow until ~0.07 s and L between 0.68 mm and 1.7 mm. First, the meniscus position in the z-direction was found at each time step, using Matlab image processing algorithms [see Fig. 8(a) for the results from 45 images of a representative WB sample]. The meniscus velocity V_m was then calculated by computing the distance covered by the meniscus (ΔL) at each time step (Δt): $V_m = \frac{\Delta L}{\Delta t}$, with $\Delta t = \frac{1}{625}$, based on the frame rate used in image capturing. The mean velocity, $\bar{V}_m$, of the advancing meniscus was calculated as the average in the x-direction and is shown in Fig. 8(b) (black rectangles) against the analytical solution $V_{m\text{-}an}$ (solid blue line). The experimental parameters n, k, σ, h, and θ_c (Tables I and II) have been used in $V_{m\text{-}an}$ for the WB sample in Fig. 8(b).
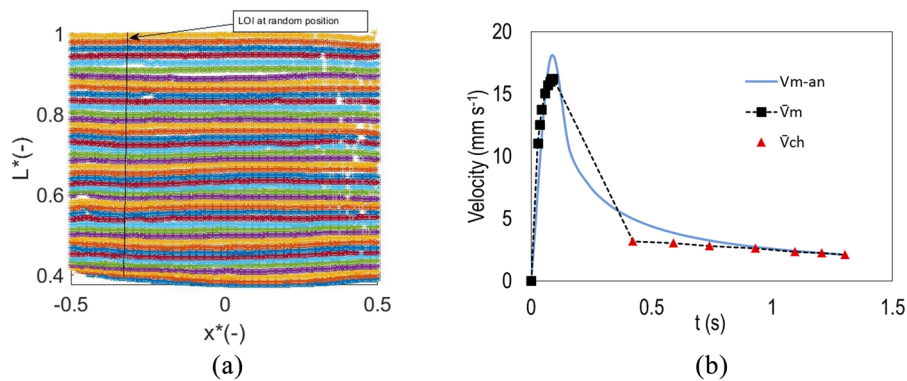
FIG. 8. (a): Normalized meniscus distance (L* = L/1.7 mm) from the entrance of the channel, across the width of the channel. (b) Mean velocity values, $\bar{V}_m$ (black rectangles) and $\bar{V}_{ch}$ (red triangles), as a function of time. The solid blue line represents the analytical solution V_{m-an} [Eq. (13)], with the first non-zero value at 0.08 s. The black dashed line connects the experimental data (not a fitted line). Data produced from a representative WB sample.

Figure 8(b) shows that the flow accelerates during the initial observation time (~0.07 s). This acceleration is mainly due to the capillary forces, which dominate over other competing, mainly viscous forces at the initial stages of the flow. This initial flow acceleration has been confirmed by the previous numerical and experimental studies in the literature.[48–50] It should be noted, here, that the analytical solution for the meniscus velocity [V_{m-an} in Eq. (13)] can capture the initial acceleration observed in the present and in other studies, only due to the initial zero velocity value at time t = 0: for very small, but non-zero values of time, the velocity magnitude will be substantially elevated to infinite values, as it is inversely proportional to this variable. For plotting purposes of V_{m-an}, in the present case, the choice of the initial time point after the zero value (t = 0.08 s) was made to avoid infinite velocities.

The dominance of the surface tension forces in the initial part of the flow is indicated by the capillary number, which was estimated using the high shear viscosity ($\mu \approx 0.006$ Pa s, Fig. 7), a mean value of 14 mm s^{-1} (from the meniscus velocity $\bar{V}_m$ in the initial stages of the flow, Fig. 8(b)), and the surface tension σ for WB (0.020 Nm^{-1}): Ca = $\frac{\mu \bar{V}_{m-mean}}{\sigma}$ = 4.2 10^{-3}. There are other forces that potentially contribute to this initial transient behavior. The fluid drop volume placed at the entrance of the channel was considerably larger than the channel volume (50 μl–0.3 μl, respectively), and the diameter of the droplet was ~6 mm. Therefore, it is reasonable to expect that an extra, albeit small, surface tension-dependent pressure contribution exists, due to the formed drop at the entrance.[4,51] Furthermore, a height difference (~3 mm) between the centers of the channel and the blood drop implies a slight hydrostatic pressure contribution (typically negligible). The aforementioned forces, although negligible, may contribute positively to the flow and may explain the meniscus acceleration during the initial stages of the flow.

When deriving the analytical solution for the meniscus velocity V_{m-an} [Eq. (13)], it was stated that the mean velocity in the core of the flow should be equal to the meniscus velocity ($\bar{V}_m$). The mean velocity in the core of the channel flow ($\bar{V}_{ch}$) was calculated from the µPIV-measured velocity profiles (the velocity profiles, V_{ch}, are presented in Sec. III B). $\bar{V}_{ch}$ is a good approximation of the meniscus velocity and was calculated by integrating the velocity profile along the x-direction, divided by the width of the channel: $\bar{V}_{ch} = \frac{1}{W} \int_{-W/2}^{W/2} V_{ch} dx$. $\bar{V}_{ch}$ was compared to the analytical solution

V_{m-an} for the meniscus velocity in the graph of Fig. 8(b) (red triangles). Quantitative differences exist between the experimental observations and analytical solution; however, a very good agreement is observed for times t > 1 s.

B. Velocity profiles in the core of the flow

Velocity profiles were extracted from the measured velocity vectors, within the region of interest shown in Fig. 3(d). The velocity vectors were averaged spatially in the z-direction and temporally for the duration of the flow (ensemble averaging) to yield the velocity profile. The resulting velocity profiles (V_{ch}) are shown in Fig. 9 for all the fluids tested. All profiles have been normalized with their maximum values ($\bar{V}_{ch}^*$), and the Newtonian analytical solution V_{z-c} [Eq. (14)] is also included for comparison. In general, the velocity profiles in the core of the flow followed the expected paraboloid behavior for all the fluids investigated, due to the no-slip conditions at the boundaries, in agreement with other capillary-driven and pressure-driven microfluidic studies.[4,11,52] Zero velocity at the side-walls has been assumed, and the velocity profiles in Fig. 9 have been extended to this value.

In Fig. 9(a), the ensemble average profiles have been calculated for the whole duration of the test (~1.6 s), and as the figure illustrates, no significant differences exist between the cases. A difference, however, is apparent between the experimental and the analytical curves. Panels (b)–(d) in Fig. 9 show the ensemble average of the velocity profiles for different time periods in the flow. As Fig. 8(b) illustrates, the velocity of the fluids decreases with time, and therefore, it is of interest to assess any time influence on the velocity profile, as it is well known that RBC aggregation is a time- and shear-dependent phenomenon.[53] The velocity profile calculated by the analytical solution is used as the reference condition. Inspecting the WB case [panel 9(b)], it is observed that the profile for the late time period (Δt_2) is blunter, when compared to the one calculated at an earlier time period Δt_1. The difference is significant for part of the channel width and can be explained by the influence of the RBC aggregation phenomenon, which is more intense at the lower shearing conditions. For the non-Newtonian fluids, the shearing forces are proportional to the velocity gradient in the flow in a non-linear manner (the power law model used in this study is an example), resulting in a higher flow resistance at the regions of lower shear.
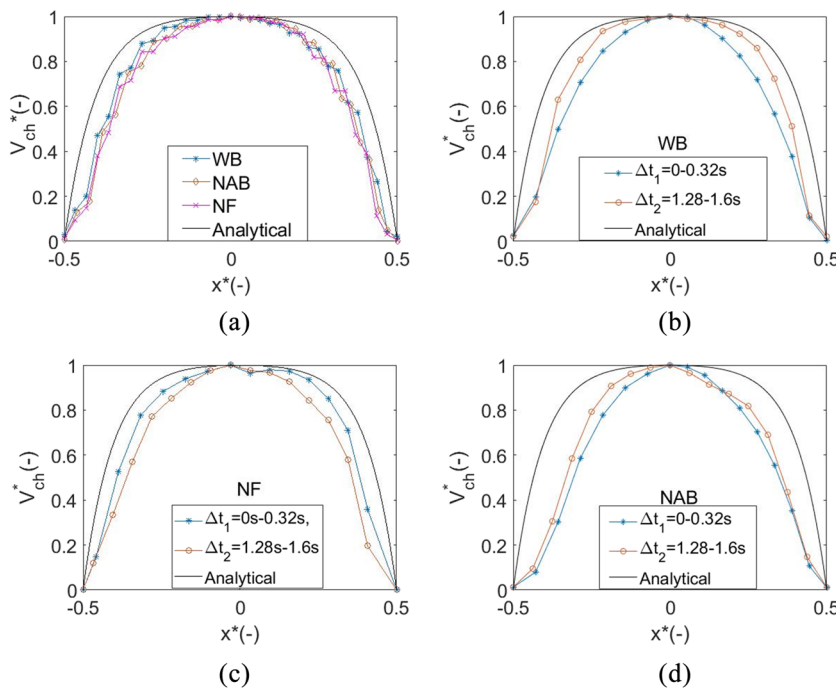
FIG. 9. Velocity profiles for WB, NAB, and NF samples at a microchannel aspect ratio of 3.5. All profiles have been normalized with the maximum velocity value in the profiles. (a) Ensemble average of the profiles of all samples for the whole duration of the flow. [(b)–(d)] Results for WB, NAB, and NF samples, respectively, for different time periods in the flow (Δt_1 and Δt_2). The analytical solution is also shown in all graphs for comparison. A zero velocity at the sidewalls has been assumed in all profiles.

Smaller differences between the profiles at the different time periods (Δt_1 and Δt_2) are observed in the other two fluids [NF and NAB, Figs. 9(c) and 9(d), respectively]. The velocity profiles for the NF case approaches the analytical one as expected. A comparison between the WB and NAB profiles shows that the velocity profile of WB is closer to the blunter, analytical profile. This is in agreement with the behavior of aggregating blood observed in previous studies:[10] in a pressure-driven flow of an aggregating blood sample in a rectangular microchannel, the velocity profile is blunter than that of the non-aggregating blood.

C. Structural characteristics

In order to estimate the extent of RBC aggregation in the measured WB flows, the intensity coefficient of variation, CV_I, was calculated as the ratio between the intensity standard deviation (SD_I) and the mean intensity ($\bar{I}$) in the ROI of the image: $CV_I = \frac{SD_I}{\bar{I}}$. RBC aggregation causes changes in the image intensity characteristics, which can be captured by the statistical variance and illustrated with CV_I. Figure 10 shows a clear difference between the aggregating case (WB) and the other two cases (NF and NAB). The CV_I for the NAB and the NF cases fluctuate around 0.23, whereas the CV of the WB case increases from 0.26 to 0.29 almost monotonically. This increase is expected as it is well known that RBC aggregation is a shear- and time-dependent function.[54]

As mentioned earlier, in previous studies[9,10] aggregating blood has shown an increase in velocity bluntness, when compared to non-aggregating samples. Large aggregates concentrate at the center of the flow resulting in an increase in viscosity, therein compared to the near wall regions.[13] The increased viscosity at the center of the channel causes a decrease in the velocity therein. Hence, the decrease

in the velocity around the center results in a blunter velocity profile. As erythrocyte aggregation is significantly influenced by inflammation sensitive properties, it may be considered as a clinically relevant parameter in this study. However, since blood from a healthy donor was used in the present study and the intensity of aggregation therein is at physiological levels, no robust conclusions can be made on the clinical significance of the phenomenon.

D. Shearing conditions

RBC aggregation is a shear- and time-dependent phenomenon, and therefore, it is of interest to estimate the shearing conditions in
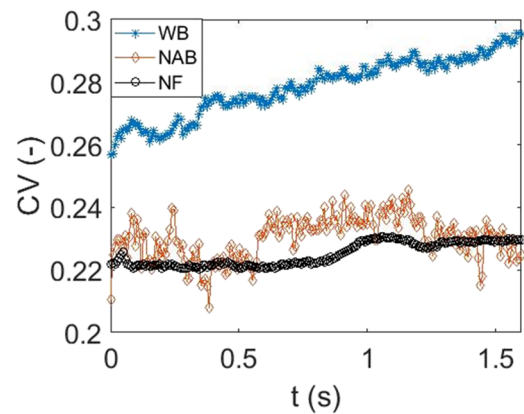

FIG. 10. Coefficient of variation of image intensity as a function of time for flow of WB, NAB, and NF samples, respectively.

the channel. The shear rate magnitude in the microchannel can be evaluated from the individual shear strain components,[55]

$$|\dot{\gamma}| = \left[2\left(\frac{\partial u}{\partial x}\right)^2 + 2\left(\frac{\partial w}{\partial z}\right)^2 + 2\left(\frac{\partial v}{\partial y}\right)^2 + \left(\frac{\partial w}{\partial x} + \frac{\partial u}{\partial z}\right)^2 \right.$$
$$\left. + \left(\frac{\partial v}{\partial z} + \frac{\partial w}{\partial y}\right)^2 + \left(\frac{\partial u}{\partial y} + \frac{\partial v}{\partial x}\right)^2 \right]^{\frac{1}{2}}. \quad (15)$$

If it is assumed that the u and v components are negligible (i.e., one-dimensional flow) and flow is fully developed ($\frac{\partial}{\partial z} = 0$); then, the equation for $|\dot{\gamma}|$ becomes

$$|\dot{\gamma}| = \left[\left(\frac{\partial w}{\partial x}\right)^2 + \left(\frac{\partial w}{\partial y}\right)^2 \right]^{\frac{1}{2}}. \quad (16)$$

The first term (the in-plane shear rate component) can be calculated from the experimental velocity profile as follows: $\dot{\gamma}_{i\text{-}p} = \frac{\partial w}{\partial x} = \frac{dV_{ch}}{dx}$. The out-of-plane shear rate component ($\dot{\gamma}_{o\text{-}p} = \frac{\partial w}{\partial y}$) was estimated as $\frac{V_{max}}{2h}$, where V_{max} is the maximum velocity in the experimental velocity profile (V_{ch}) and 2h is the channel height (100 μm). $|\dot{\gamma}|$ is shown in Fig. 11 as fitted curves on the experimental data. Moderate to strong shear conditions occur closer to the walls reaching magnitudes of more than 90 s^{-1}. Studies on normal RBC aggregation kinetics in shear flow[56] have shown that for healthy human RBCs, the disaggregation process starts from $\dot{\gamma} = 2.5$ s^{-1}, whereas other studies[57] have shown that a critical disaggregation shear rate lies between $\dot{\gamma} \sim 70$ s^{-1} and 150 s^{-1}. Furthermore, since the µPIV technique underestimates the calculated velocities, the actual shearing conditions are expected to be further elevated.

Therefore, the shear conditions developed in the microchannel, especially close to the walls and during the initial time periods, are sufficiently strong to keep RBC aggregation at low levels. The value of CV_I (Fig. 10) of the aggregating sample increased ~15% compared to the PBS value at the initial stages of the flow, reaching a difference of ~27% at the final stages.

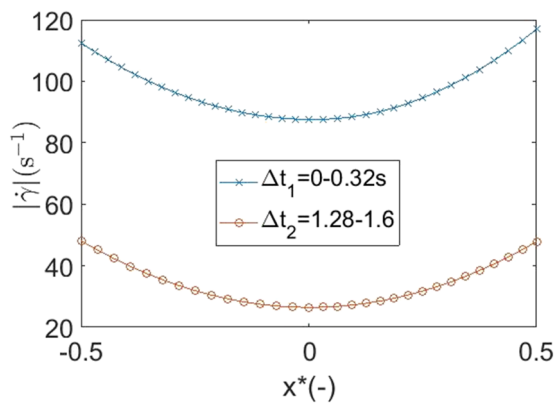**FIG. 11**. Profiles of $|\dot{\gamma}|$ across the width of the channel at two different time periods Δt_1 and Δt_2 (lines fitted on experimental data).

E. Limitations

In the bright field µPIV technique, there is a certain degree of error due to the large depth of correlation of the microscope objective. This finite depth of correlation leads to an underestimation of the velocity magnitude, the extent of which was assessed in the present study and agrees with the previous reports (discussed earlier in Sec. II F). Nevertheless, as it can be observed in Fig. 5, the velocity underestimation is seen to be consistent across the flow field, and therefore, the shape of the velocity profile should be qualitatively preserved.

The side-walls of the channel are constructed by using a double-sided adhesive tape, which introduces an apparent roughness on the side-wall–flow interface. As a result, an uncertainty in the exact location of the wall exists, and the local flow may be influenced in this region. For this reason, the PIV analysis was performed on the flow field indicated by the ROI in Fig. 3(d), and the velocity profiles were extended to an assumed zero value (no slip) at the walls of the channel, i.e., at x* = 0.5.

The sample deposition at the entrance of the channel is conducted with great care by the trained operator using a micropipette. The sample volume is consistently controlled using the micropipette; however, uncertainties due to sample handling might be possible. In the present work, cases showing abnormal behavior (mainly abnormal meniscus velocity at the entrance) have been excluded from the analysis.

Viscosity values at the lowest shear rate (12.5 s^{-1}) were close to the lower sensitivity limit of the viscometer (accepted at the 5% of the transducer torque range). Nevertheless, the viscosity of the Newtonian fluid measured in this low-end of the torque sensitivity shows no significant deviation from the rest of the values, indicating valid readings of viscosity for WB and NAB fluids.

IV. CONCLUSIONS

In the present study, the influence of red blood cell aggregation on surface tension driven flows in a rectangular microchannel was examined. A Newtonian fluid and non-aggregating and aggregating blood samples were tested, and the flow characteristics in the microchannel were analyzed and compared, through micro-PIV-based techniques and analytical solutions. RBC aggregation was found to have an influence on the flow characteristics as manifested by the velocity profile bluntness. Moderate to strong shear rates were observed in the initial stages of the flow, determining the extent of aggregation present in the channel. The present results illustrate that RBC aggregation should be considered as an influencing factor in passive microchannel blood flows akin to those used in many point of care diagnostics.

AUTHORS' CONTRIBUTIONS

D.P., A.P., G.C., S.B., and E.K. contributed equally to this work.

ACKNOWLEDGMENTS

DATA AVAILABILITY

The data that support the findings of this study are available from the corresponding author upon reasonable request.

REFERENCES

[1] E. K. Sackmann, A. L. Fulton, and D. J. Beebe, "The present and future role of microfluidics in biomedical research," Nature **507**, 181 (2014).

[2] B. Weigl, G. Domingo, P. Labarre, and J. Gerlach, "Towards non- and minimally instrumented, microfluidics-based diagnostic devices," Lab Chip **8**, 1999 (2008).

[3] J. H. Tsui, W. Lee, S. H. Pun, J. Kim, and D.-H. Kim, "Microfluidics-assisted in vitro drug screening and carrier production," Adv. Drug Deliv. Rev. **65**, 1575 (2013).

[4] E. Berthier and D. J. Beebe, "Flow rate analysis of a surface tension driven passive micropump," Lab Chip **7**, 1475 (2007).

[5] J. G. Santiago, S. T. Wereley, C. D. Meinhart, D. J. Beebe, and R. J. Adrian, "A particle image velocimetry system for microfluidics," Exp. Fluids **25**, 316 (1998).

[6] A. G. Koutsiaris, D. S. Mathioulakis, and S. Tsangaris, "Microscope PIV for velocity-field measurement of particle suspensions flowing inside glass capillaries," Meas. Sci. Technol. **10**, 1037 (1999).

[7] R. Lima, S. Wada, K.-i. Tsubota, and T. Yamaguchi, "Confocal micro-PIV measurements of three-dimensional profiles of cell suspension flow in a square microchannel," Meas. Sci. Technol. **17**, 797 (2006).

[8] R. Lima, T. Ishikawa, Y. Imai, M. Takeda, S. Wada, and T. Yamaguchi, "Radial dispersion of red blood cells in blood flowing through glass capillaries: The role of hematocrit and geometry," J. Biomech. **41**, 2188 (2008).

[9] J. M. Sherwood, J. Dusting, E. Kaliviotis, and S. Balabani, "The effect of red blood cell aggregation on velocity and cell-depleted layer characteristics of blood in a bifurcating microchannel," Biomicrofluidics **6**, 024119 (2012).

[10] J. M. Sherwood, E. Kaliviotis, J. Dusting, and S. Balabani, "Hematocrit, viscosity and velocity distributions of aggregating and non-aggregating blood in a bifurcating microchannel," Biomech. Model. Mechanobiol. **13**, 259 (2014).

[11] J. M. Sherwood, D. Holmes, E. Kaliviotis, and S. Balabani, "Spatial distributions of red blood cells significantly alter local haemodynamics," PLoS One **9**, e100473 (2014).

[12] E. Kaliviotis, D. Pasias, J. M. Sherwood, and S. Balabani, "Red blood cell aggregate flux in a bifurcating microchannel," Med. Eng. Phys. **48**, 23 (2016).

[13] E. Kaliviotis, J. M. Sherwood, and S. Balabani, "Partitioning of red blood cell aggregates in bifurcating microscale flows," Sci. Rep. **7**, 44563 (2017).

[14] E. Kaliviotis, J. M. Sherwood, and S. Balabani, "Local viscosity distribution in bifurcating microfluidic blood flows," Phys. Fluids **30**, 030706 (2018).

[15] G. Tomaiuolo, L. Lanotte, G. Ghigliotti, C. Misbah, and S. Guido, "Red blood cell clustering in Poiseuille microcapillary flow," Phys. Fluids **24**, 051903 (2012).

[16] R. D'Apolito, F. Taraballi, S. Minardi, X. Liu, S. Caserta, A. Cevenini, E. Tasciotti, G. Tomaiuolo, and S. Guido, "Microfluidic interactions between red blood cells and drug carriers by image analysis techniques," Med. Eng. Phys. **38**, 17 (2016).

[17] R. Mehri, J. Laplante, C. Mavriplis, and M. Fenech, "Investigation of blood flow analysis and red blood cell aggregation," J. Med. Biol. Eng. **34**, 469 (2014).

[18] R. Mehri, C. Mavriplis, and M. Fenech, "Red blood cell aggregates and their effect on non-Newtonian blood viscosity at low hematocrit in a two-fluid low shear rate microfluidic system," PLoS One **13**, e0199911 (2018).

[19] W. H. Reinhart, N. Z. Piety, and S. S. Shevkoplyas, "Influence of red blood cell aggregation on perfusion of an artificial microvascular network," Microcirculation **24**, e12317 (2016).

[20] J. Berthier, K. A. Brakke, E. P. Furlani, I. H. Karampelas, V. Poher, D. Gosselin, M. Cubizolles, and P. Pouteau, "Whole blood spontaneous capillary flow in narrow V-groove microchannels," Sens. Actuators, B **206**, 258 (2015).

[21] S. Cito, Y.-C. Ahn, J. Pallares, R. M. Duarte, Z. Chen, M. Madou, and I. Katakis, "Visualization and measurement of capillary-driven blood flow using spectral domain optical coherence tomography," Microfluid. Nanofluidics **13**, 227 (2012).

[22] H. D. Gesser and P. Krause, "A demonstration of surface tension and contact angle," J. Chem. Educ. **77**(1), 58 (2000).

[23] C. K. Chung, Y. S. Chen, and T. R. Shih, "Fabrication and flow test of long-term hydrophilic fluidic chip without using any surface modification treatment," Microfluid. Nanofluidics **6**, 853 (2009).

[24] B. Ruben, M. Elisa, L. Leandro, M. Victor, G. Gloria, S. Marina, S. Mian K, R. Pandiyan, and L. Nadhira, "Oxygen plasma treatments of polydimethylsiloxane surfaces: effect of the atomic oxygen on capillary flow in the microchannels," Micro Nano Lett. **12**, 754 (2017).

[25] A. U. Alam, M. M. R. Howlader, and M. J. Deen, "The effects of oxygen plasma and humidity on surface roughness, water contact angle and hardness of silicon, silicon dioxide and glass," J. Micromech. Microeng. **24**, 035010 (2014).

[26] S. Luo and C. P. Wong, "Effect of UV/ozone treatment on surface tension and adhesion in electronic packaging," IEEE Trans. Components Packag. Technol. **24**, 43 (2001).

[27] M. Sneha Maria, P. E. Rakesh, T. S. Chandra, and A. K. Sen, "Capillary flow of blood in a microchannel with differential wetting for blood plasma separation and on-chip glucose detection," Biomicrofluidics **10**, 054108 (2016).

[28] H. M. Kim, S. B. Seo, D. Y. Kim, K. Bae, and S. Y. Sohn, "Enhanced hydrophilic property of TiO$_2$ thin film deposited on glass etched with O$_2$ plasma," Trans. Electr. Electron. Mater. **14**, 152 (2013).

[29] Y.-F. Chen, F.-G. Tseng, S.-Y. ChangChien, M.-H. Chen, R.-J. Yu, and C.-C. Chieng, "Surface tension driven flow for open microchannels with different turning angles," Microfluid. Nanofluidics **5**, 193 (2008).

[30] C. F. Kung, C. F. Chiu, C. F. Chen, C. C. Chang, and C. C. Chu, "Blood flow driven by surface tension in a microchannel," Microfluid. Nanofluidics **6**, 693 (2009).

[31] N. Ichikawa, K. Hosokawa, and R. Maeda, "Interface motion of capillary-driven flow in rectangular microchannel," J. Colloid Interface Sci. **280**, 155 (2004).

[32] W. Huang, R. S. Bhullar, and Y. C. Fung, "The surface-tension-driven flow of blood from a droplet into a capillary tube," J. Biomech. Eng. **123**, 446 (2001).

[33] S. Chakraborty, "Dynamics of capillary flow of blood into a microfluidic channel," Lab Chip **5**, 421 (2005).

[34] J. Wang, W. Huang, R. S. Bhullar, and P. Tong, "Modeling of surface-tension-driven flow of blood in capillary tubes," Mech. Chem. Biosyst. **1**, 161 (2004).

[35] K. Lee, M. Kinnunen, M. D. Khokhlova, E. V. Lyubin, A. V. Priezzhev, I. Meglinski, and A. A. Fedyanin, "Optical tweezers study of red blood cell aggregation and disaggregation in plasma and protein solutions," J. Biomed. Opt. **21**, 035001 (2016).

[36] O. K. Baskurt and H. J. Meiselman, "Blood rheology and hemodynamics," Semin. Thromb. Hemost. **29**, 435 (2003).

[37] W. Kowalczyk, B. E. Zima, and A. Delgado, "A biological seeding particle approach for µ-PIV measurements of a fluid flow provoked by microorganisms," Exp. Fluids **43**, 147 (2007).

[38] D. Juncker, H. Schmid, U. Drechsler, H. Wolf, M. Wolf, B. Michel, N. De Rooij, and E. Delamarche, "Autonomous microfluidic capillary system," Anal. Chem. **74**, 6139 (2002).

[39] S. Cito, J. Pallares, A. Fabregat, and I. Katakis, "Numerical simulation of wall mass transfer rates in capillary-driven flow in microchannels," Int. Commun. Heat Mass Transfer **39**, 1066 (2012).

[40] Y. Yuan and T. R. Lee, *Surface Science Techniques* (Springer, Berlin, Heidelberg, 2013), pp. 3–5.

[41] C. J. Bourdon, M. G. Olsen, and A. D. Gorby, "The depth of correlation in micro-PIV for high numerical aperture and immersion objectives," J. Fluids Eng. **128**, 883 (2006).

[42]C. Poelma, A. Kloosterman, B. P. Hierck, and J. Westerweel, "Accurate blood flow measurements: Are artificial tracers necessary," PLoS One **7**, e45247 (2012).

[43]S. Zhang, N. Cagney, S. Balabani, C. P. Naveira-Cotta, and M. K. Tiwari, "Probing vortex-shedding at high frequencies in flows past confined microfluidic cylinders using high-speed microscale particle image velocimetry," Phys. Fluids **31**, 102001 (2019).

[44]S. Zhang, N. Cagney, T. Lacassagne, S. Balabani, S. Naveira-Cotta, and M. K. Tiwaria, "Mixing in flows past confined microfluidic cylinders: Effects of pin and fluid interface offsetting," Chem. Eng. J. **397**, 125358 (2020).

[45]C. T. Crowe, J. D. Schwarzkopf, M. Sommerfeld, and Y. Tsuji, *Multiphase Flows with Droplets and Particles* (CRC Press, Boca Raton, FL, 2011).

[46]M. A. Elblbesy and A. T. Hereba, "Computation of the coefficients of the power law model for whole blood and their correlation with blood parameters," Appl. Phys. Res. **8**, 1 (2016).

[47]H. Bruus, *Theoretical Microfluidics* (Oxford University Press, USA, 2008).

[48]G. Cavaccini, V. Pianese, A. Jannelli, S. Iacono, and R. Fazio, "One-dimensional mathematical and numerical modeling of liquid dynamics in a horizontal capillary," J. Comput. Methods Sci. Eng. **9**, 3 (2009).

[49]J. Szekely, A. W. Neumann, and Y. K. Chuang, "The rate of capillary penetration and the applicability of the washburn equation," J. Colloid Interface Sci. **35**, 273 (1971).

[50]N. Srivastava and M. A. Burns, "Analysis of non-Newtonian liquids using a microfluidic capillary viscometer," Anal. Chem. **78**, 1690 (2006).

[51]S. Zaitsev, "Dynamic surface tension measurements as general approach to the analysis of animal blood plasma and serum," Adv. Colloid Interface Sci. **235**, 201 (2016).

[52]A. R. Pries, D. Neuhaus, and P. Gaehtgens, "Blood viscosity in tube flow: Dependence on diameter and hematocrit," Am. J. Physiol. - Heart Circ. Physiol. **263**, H1770 (1992).

[53]E. Kaliviotis and M. Yianneskis, "On the effect of microstructural changes of blood on energy dissipation in Couette flow," Clin. Hemorheol. Microcirc. **39**, 235 (2008).

[54]E. Kaliviotis and M. Yianneskis, "An energy-rate based blood viscosity model incorporating aggregate network dynamics," Biorheology **46**, 487 (2009).

[55]E. Kaliviotis, J. Dusting, and S. Balabani, "Spatial variation of blood viscosity: Modelling using shear fields measured by a μPIV based technique," Med. Eng. Phys. **33**, 824 (2011).

[56]A. V. Priezzhev, O. M. Ryaboshapka, N. N. Firsov, and I. V. Sirko, "Aggregation and disaggregation of erythrocytes in whole blood: Study by backscattering technique," J. Biomed. Opt. **4**(1), 76 (1999).

[57]P. Snabre, M. Bitbol, and P. Mills, "Cell disaggregation behavior in shear flow," Biophys. J. **51**, 795 (1987).